ACS OMEGA

Article

Cite This: ACS Omega 2017, 2, 7039-7047

http://pubs.acs.org/journal/acsodf

Highly Active Tungsten Oxide Nanoplate Electrocatalysts for the Hydrogen Evolution Reaction in Acidic and Near Neutral Electrolytes

Arpan Kumar Nayak,[†] Manju Verma,[‡] Youngku Sohn,[§] Parag A. Deshpande,[‡] and Debabrata Pradhan*[,†]

[†]Materials Science Centre and [‡]Quantum and Molecular Engineering Laboratory, Department of Chemical Engineering, Indian Institute of Technology, Kharagpur, West Bengal 721 302, India

[§]Department of Chemistry, Chungnam National University, Yuseong-gu, Daejeon 34134, Republic of Korea

Supporting Information

ABSTRACT: An efficient, cost-effective, and earth-abundant catalyst that could drive the production of hydrogen from water without or with little external energy is the ultimate goal toward hydrogen economy. Herein, nanoplates of tungsten oxide and its hydrates ($WO_3 \cdot H_2O$) as promising electrocatalysts for the hydrogen evolution reaction (HER) are reported. The square-shaped and stacked $WO_3 \cdot H_2O$ nanoplates are synthesized at room temperature under air in ethanol only, making it as a promising green synthesis strategy. The repeated electrochemical cyclic voltammetry cycles modified the surface of $WO_3 \cdot H_2O$ nanoplates to WO_3 as confirmed by X-ray photoelectron and Auger spectroscopy, which leads to an improved HER activity. Hydrogen evolution is further achieved from distilled water (pH 5.67) producing 1 mA cm^{-2} at an overpotential of 15 mV versus the reversible hydrogen electrode. Moreover, $WO_3 \cdot H_2O$ and WO_3 nanoplates demonstrate excellent durability in acidic and neutral media, which is highly desirable for practical application. Improved hydrogen evolution by WO_3(200) when compared to that by Pt(111) is further substantiated by the density functional theory calculations.

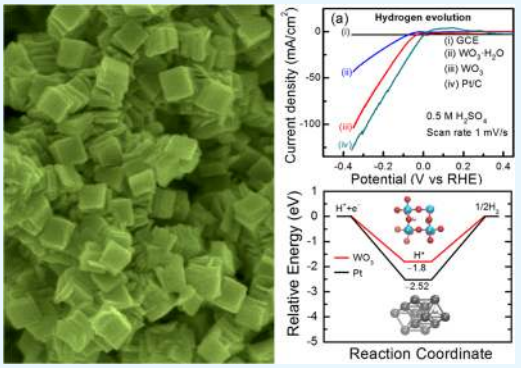

INTRODUCTION

Rapid depletion of fossil fuels and ever-increasing energy demand prompt the researchers to explore clean, renewable, sustainable, and environmentally friendly energy sources.[1] On that prospect, hydrogen is considered as an efficient, earth-abundant, and renewable clean energy carrier that has potential to play a major role. Hydrogen can be produced through electrochemical water splitting with zero emission of CO_2, which makes the process green and sustainable.[2] Two important half reactions of water splitting are the hydrogen evolution reaction (HER), that is, $2H^+(aq) + 2e^- \rightarrow H_2(g)$ and the oxygen evolution reaction, that is, $2H_2O(l) \rightarrow O_2(g) + 4H^+(aq) + 4e^-$, occurring at the cathode and the anode, respectively.[3] To lower the overpotential of these reactions while increasing their reaction rate, electrocatalysts at the cathode and anode surface play the central role, thus improving the overall efficiency of the water-splitting reaction. Noble metals such as platinum (Pt), palladium (Pd), and ruthenium (Ru) have so far been recognized as effective and efficient HER catalysts with negligible overpotential and excellent kinetics in acidic electrolyte solutions.[4,5] However, high cost and poor earth-abundance of these noble metals are the major hindrance for their practical utilization.[6,7] Therefore, it is indispensable to develop noble metal-free HER catalysts which are not only efficient but also earth-abundant, low cost, and stable in the electrolyte which is being used. Several noble metal-free electrocatalysts, particularly Mo- and W-based materials, have been reported recently and have been reckoned to be promising. In particular, chalcogenides such as MoS_2,[8−12] WS_2,[13−16] WSe_2,[17] and $MoSe_2$[17] have been successfully investigated as cost-effective potential substitution to the noble metal-based catalysts in acidic solutions. Although several chalcogenides have been studied for the HER in acidic media, little emphasis has been directed toward metal hydroxides and/or oxides and/or in neutral media.

Hydrogen evolution in neutral electrolyte solutions is desirable for practical applications. Thus, 0.1 M acetate buffer solution (pH 4.5) and phosphate buffer solution (PBS, pH 7) have been used as electrolytes for hydrogen evolution by Andreiadis et al.[18] with a cobalt-based complex and Karunadasa et al.[19] with a molybdenum-oxo-complex, respectively. Helm et al. also demonstrated hydrogen production using nickel complexes in both aqueous and acidic electrolytes.[20] The synthesis of these metal complexes is not only complex but also involves multiple steps and several chemicals. However, the stability of these complexes for long-term uses is an issue. Therefore, it is of immense importance to explore suitable

Received: August 8, 2017
Accepted: October 9, 2017
Published: October 20, 2017

DOI: 10.1021/acsomega.7b01151
ACS Omega 2017, 2, 7039−7047

inorganic electrocatalysts for hydrogen generation in neutral media.

Here, competent HER activity of tungsten trioxide (WO_3) nanoplates is demonstrated in acidic and neutral electrolytes, and compared with standard platinum on carbon (Pt/C) catalysts. Coincidently, WO_3 was obtained by electrochemical surface oxidization of $WO_3{\cdot}H_2O$ nanoplates through repeated electrochemical cyclic voltammetry (CV) cycles for the first time. The electrochemically surface-modified $WO_3{\cdot}H_2O$ exhibits a performance similar to WO_3 obtained separately by annealing $WO_3{\cdot}H_2O$ nanoplates under air at 400 °C. It is noteworthy that $WO_3{\cdot}H_2O$ nanoplates were synthesized at room temperature using only ethanol as a solvent thus excluding the use of corrosive HCl or HNO_3 along with other organic chemicals previously reported for the synthesis of hydrated WO_3.[21−24] To demonstrate the potential of the present electrocatalysts, we further demonstrate hydrogen evolution in a neutral medium (distilled water; pH, 5.67) and their remarkable stabilities in acidic and neutral electrolytes. The superior HER activity of WO_3 when compared to that of Pt is additionally supported by reaction energetics obtained by the density functional theory (DFT) calculations.

RESULTS AND DISCUSSION

Structural Analysis. The structural analysis of the as-synthesized samples was carried out by powder X-ray diffraction (XRD) as shown in Figure 1. The diffraction

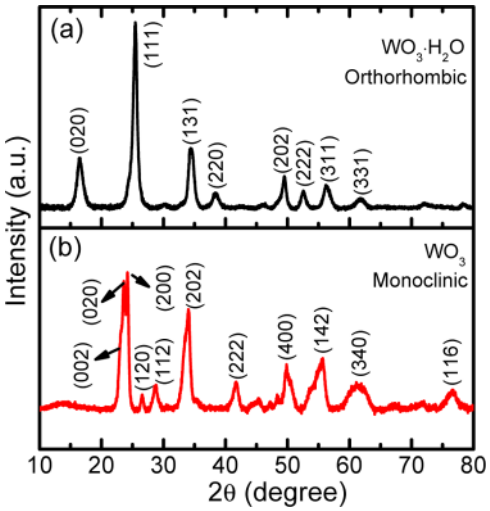

Figure 1. XRD patterns of (a) orthorhombic $WO_3{\cdot}H_2O$ nanoplates and (b) monoclinic WO_3 nanoplates obtained by annealing $WO_3{\cdot}H_2O$ at 400 °C for 2 h under air.

features of the precipitate formed at room temperature (Figure 1a) are readily indexed to the orthorhombic $WO_3{\cdot}H_2O$ with lattice parameters a = 5.25 Å, b = 10.7 Å, and c = 5.11 Å, which are in good agreement with those of JCPDS file no. 00-043-0679 (a = 5.24 Å, b = 10.7 Å, and c = 5.12 Å). The XRD pattern (Figure 1b) of $WO_3{\cdot}H_2O$ annealed at 400 °C for 2 h under air matches that of monoclinic WO_3 with lattice parameters a = 7.3 Å, b = 7.51 Å, and c = 7.71 Å (JCPDS file no. 01-083-0951, a = 7.3 Å, b = 7.54 Å, and c = 7.69 Å). No other phases and/or impurities such as $WO_3{\cdot}2H_2O$ and $WO_3{\cdot}0.33H_2O$ were found in any of these samples indicating the phase-pure product. The XRD analysis suggests that the $WO_3{\cdot}H_2O$ powder formed at room temperature is completely phase-transformed to WO_3 upon annealing at 400 °C for 2 h under air.

Thermal Stability. Complete conversion of $WO_3{\cdot}H_2O$ to WO_3 upon annealing was further confirmed by thermogravimetry (TG) analysis. Figure 2 shows the TG and its derivative

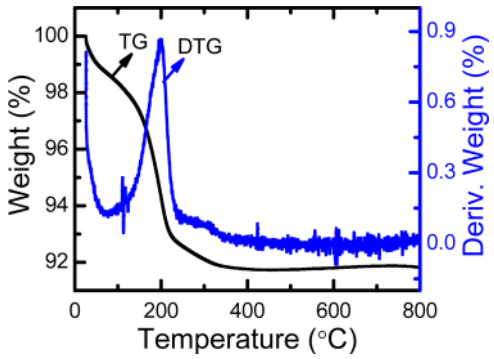

Figure 2. TG curve and its derivative plot of $WO_3{\cdot}H_2O$ nanoplates performed under air with a heating rate of 10 °C min^{-1}.

plot of $WO_3{\cdot}H_2O$ nanoplates in a temperature range of 26−800 °C at a heating rate of 10 °C min^{-1} under air. A major weight loss of 7.2% occurred up to 230 °C matches the theoretical value of 7.2% confirming the phase transformation of $WO_3{\cdot}H_2O$ to WO_3.[25] The subsequent weight loss of 1.1% between 230 and 400 °C is believed to be due to the final water decomposition in the crystallization of minor amorphous contents.[23] The TG analysis corroborates the XRD results on the complete phase transformation of $WO_3{\cdot}H_2O$ to WO_3 under air at 400 °C for 2 h (Figure 1).

Morphology and Microstructure. The morphology and microstructure of the as-synthesized orthorhombic $WO_3{\cdot}H_2O$ and monoclinic WO_3 were examined in detail using field emission scanning electron microscopy (FESEM) and transmission electron microscopy (TEM), respectively. Figure 3a,b shows the FESEM images of $WO_3{\cdot}H_2O$ nanoplates at different magnifications synthesized by mixing WCl_6 in ethanol at room temperature. These nanoplates were found to be square-shaped, highly uniform, and stacked. The length/width of these nanoplates was measured to be 100 nm with a thickness <30 nm, measured from the magnified SEM image (shown as an inset in Figure 3b). Figure 3c presents a TEM image of stacked $WO_3{\cdot}H_2O$ nanoplates in accordance with the FESEM images. The high-resolution TEM (HRTEM) image of a $WO_3{\cdot}H_2O$ nanoplate shows a lattice spacing of 3.5 Å corresponding to the (111) plane as shown in Figure 3d. Additional TEM images (Figure S1, Supporting Information) clearly depict the stacked arrangement and thickness of individual $WO_3{\cdot}H_2O$ nanoplates. The powder XRD pattern (Figure 1a) of $WO_3{\cdot}H_2O$ nanoplates also shows maximum intensity for the same (111) plane indicating their growth direction. The regular spot selected area diffraction (SAED) pattern (inset of Figure 3d) obtained from the $WO_3{\cdot}H_2O$ nanoplate confirms its single crystalline nature. Although synthesis of $WO_3{\cdot}H_2O$ nanoplates has been reported earlier,[21,23,24] they were of much larger sizes and synthesized at a higher temperature than the room temperature used in the present work. In particular, Huang et al.[23] synthesized rectangular slab-like $WO_3{\cdot}H_2O$ of size 2−3 μm by taking Na_2WO_4 and HCl at 70 °C for 10 h and Kalantar-zadeh et al.[24] reported hydrated WO_3 platelets of 0.2−2 μm size obtained at 80 °C for 6 h using 0.5 M HNO_3. Recently, Guo et al. reported

DOI: 10.1021/acsomega.7b01151
ACS Omega 2017, 2, 7039−7047

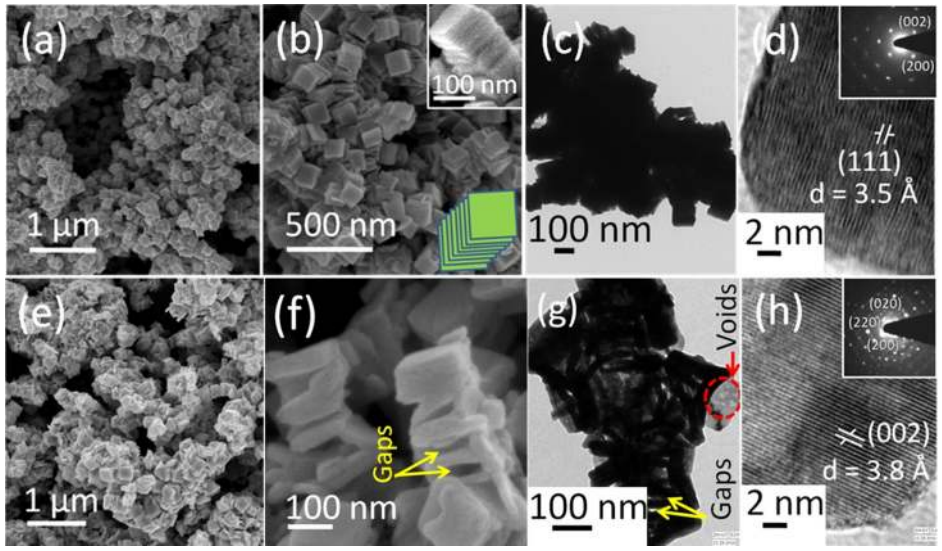

Figure 3. FESEM images of (a,b) square-shaped $WO_3 \cdot H_2O$ nanoplates of length/width 100 nm, synthesized by just mixing WCl_6 in ethanol under ambient conditions, inset of (b) shows the corresponding magnified image revealing stacked arrangement of nanoplates, and (c) TEM and (d) HRTEM images of $WO_3 \cdot H_2O$ nanoplates. Inset of (d) shows a SAED pattern of $WO_3 \cdot H_2O$ nanoplates. FESEM images of (e,f) WO_3 nanoplates obtained by calcining $WO_3 \cdot H_2O$ at 400 °C for 2 h. (g) TEM and (h) HRTEM images of WO_3 nanoplates. Inset of (h) shows a SAED pattern of WO_3 nanoplates.

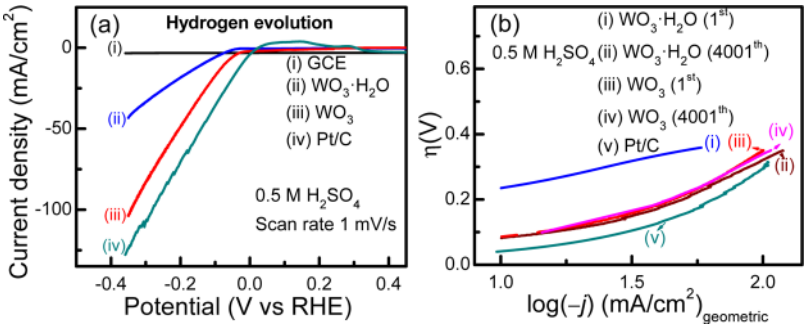

Figure 4. (a) LSV and (b) Tafel plots of $WO_3 \cdot H_2O$ and WO_3 nanoplates for the HER in 0.5 M H_2SO_4.

orthorhombic $WO_3 \cdot H_2O$ nanoplates of size >200 nm by the hydrothermal method at 100 °C for 10 h.[21] The formation of nanosized $WO_3 \cdot H_2O$ plates (~100 nm) is thus attributed to the lower synthesis temperature (room temperature) employed in the present work. Figure 3e,f shows the FESEM images of stacked WO_3 nanoplates at different magnifications obtained by annealing $WO_3 \cdot H_2O$ nanoplates at 400 °C for 2 h under air. The annealing not only produced phase-pure WO_3 but also resulted in nanoplates to be separated in the stack as shown in Figure 3f. A TEM image of WO_3 nanoplates is shown in Figure 3g, which reveals the formation of gap between consecutive nanoplates (marked by arrows) and voids (marked by a circle) in the nanoplates. The formation of gaps and voids in WO_3 nanoplates is due to the annealing of $WO_3 \cdot H_2O$ nanoplates at a higher temperature (400 °C). In $WO_3 \cdot H_2O$, water molecules are present between layers of WO_6 octahedral units and the $W-OH_2$ bond is weak.[26,27] Thus, water molecules in $WO_3 \cdot H_2O$ nanoplates are evaporated upon annealing as confirmed from the mass loss (Figure 2) forming gaps between nanoplates and voids in the resulting WO_3 nanoplates. The HRTEM image of a WO_3 nanoplate shows a lattice spacing of 3.8 Å, corresponding to the (002) plane of monoclinic WO_3. The regular spot SAED pattern (inset of Figure 3h) confirmed the single crystalline nature of the WO_3 nanoplates. In addition, the elemental energy dispersive X-ray (EDX) mapping of $WO_3 \cdot H_2O$ and WO_3 nanoplates was performed (Figure S2, Supporting Information) in a FESEM which shows a uniform distribution of W and O throughout the sample.

Electrocatalytic HER Study. The electrochemical HER performance of $WO_3 \cdot H_2O$ and WO_3 nanoplates was examined by linear sweep voltammetry (LSV), CV, and chronoamperometry in a highly acidic (0.5 M H_2SO_4) electrolyte. Figure 4a presents the LSV plots for the HER in 0.5 M H_2SO_4 at 1 mV s^{-1} with $WO_3 \cdot H_2O$ and WO_3 nanoplates along with Pt/C and glassy carbon electrodes (GCE) for comparison. An overpotential of 147, 73, and 24 mV was measured to obtain 10 mA cm^{-2} with $WO_3 \cdot H_2O$, WO_3, and Pt/C, respectively. An 73 mV overpotential with WO_3 nanoplates was found to be smaller than that reported for several nonnoble metal electrocatalysts including Ni_2P (117 mV),[28] MoS_2/Au (226 mV),[29] MoS_2 (190 mV),[30] WS_2 (233 mV),[13] and other electrocatalysts (Table S1, Supporting Information). Moreover, a similar superior HER activity was reported by Phuruangrat et al. with hexagonal WO_3 nanowires synthesized by the microwave-assisted hydrothermal method.[31] This suggests WO_3 as a potential HER electrocatalyst. The cyclic stability of $WO_3 \cdot H_2O$ and WO_3 nanoplates was tested by performing CV for 4000 cycles in 0.5 M H_2SO_4 at 100 mV s^{-1} (Figure S3, Supporting Information). A slight

DOI: 10.1021/acsomega.7b01151
ACS Omega 2017, 2, 7039−7047

Table 1. HER Performance of $WO_3 \cdot H_2O$ and WO_3 Nanoplates in Different Electrolytes

catalysts	electrolyte	overpotential (mV at 10 mA cm^{-2} vs RHE)	Tafel slope (mV dec^{-1})	exchange current density (A cm^{-2})
$WO_3 \cdot H_2O$ (1st LSV)	0.5 M H_2SO_4	147	43.9	6.11×10^{-3}
WO_3 (1st LSV)	0.5 M H_2SO_4	73	39.5	12.58×10^{-3}
$WO_3 \cdot H_2O$ (4001st LSV)	0.5 M H_2SO_4	66	34.8	14.2×10^{-3}
WO_3 (4001st LSV)	0.5 M H_2SO_4	70	38.53	12.82×10^{-3}
Pt/C	0.5 M H_2SO_4	24	29	17.78×10^{-3}
$WO_3 \cdot H_2O$ (1st LSV)	distilled water		55.7	0.02×10^{-3}
WO_3 (1st LSV)	distilled water	331 at 1 mA cm^{-2}	51.59	0.021×10^{-3}
$WO_3 \cdot H_2O$ (10001st LSV)	distilled water	177 at 1 mA cm^{-2}	32	0.032×10^{-3}
WO_3 (10001st LSV)	distilled water	193 at 1 mA cm^{-2}	47.73	0.052×10^{-3}

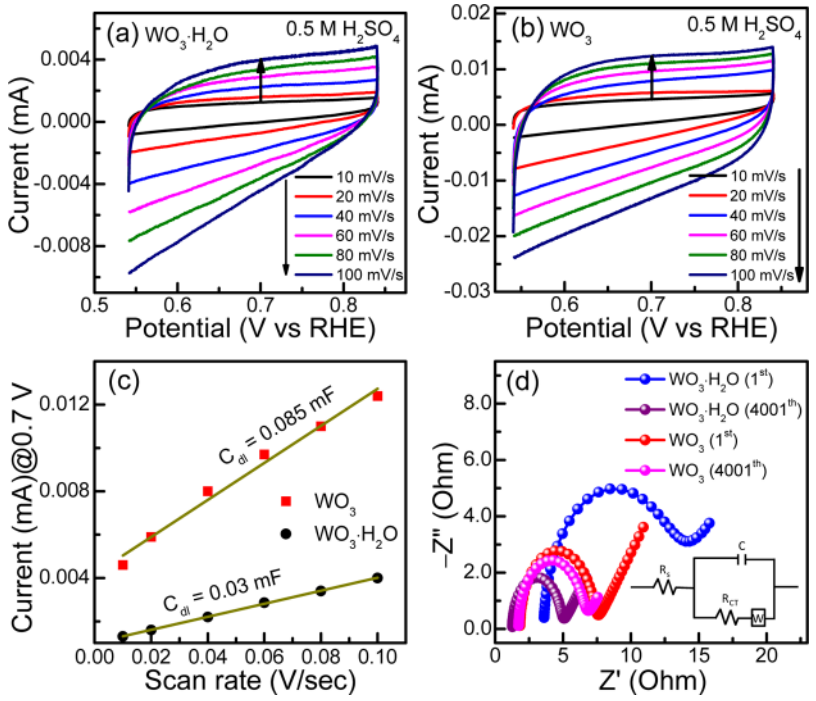

Figure 5. CVs at different scan rates in the potential range of 0.54−0.84 V vs the RHE (nonfaradaic region) in 0.5 M H_2SO_4 solution with (a) $WO_3 \cdot H_2O$ and (b) WO_3 nanoplates. (c) Capacitive currents measured at 0.7 V vs the RHE as a function of scan rates with $WO_3 \cdot H_2O$ and WO_3 nanoplates. (d) Nyquist plots of $WO_3 \cdot H_2O$ and WO_3 nanoplates at 0.06 V (vs RHE) before and after the stability test and the inset shows the equivalent circuit diagram used to fit the experimental data.

positive current on Pt/C, $WO_3 \cdot H_2O$, and WO_3 prior to onset potential of the HER (Figure 4a) was found to disappear after CV cycles, which is believed to be due to oxidative surface cleaning and surface oxidation of hydroxide. Furthermore, the HER current density of $WO_3 \cdot H_2O$ was found to be significantly increased (Figure S3a) with repeated CV cycles toward the value of WO_3 nanoplates (Figure S3b), which is attributed to surface oxidation of $WO_3 \cdot H_2O$ to WO_3 (discussed later). A smaller increase in the HER current density for WO_3 nanoplates (Figure S3b) can be termed to surface cleaning during CV cycles and conversion of surface hydroxide to oxide.[17] Figure 4b shows the Tafel plots of the electrocatalysts from which a slope was measured. The Tafel slopes (and exchange current densities) were measured to be 43.9 mV dec^{-1} (6.1 mA cm^{-2}), 39.5 mV dec^{-1} (12.58 mA cm^{-2}), and 29 mV dec^{-1} (17.78 mA cm^{-2}) for $WO_3 \cdot H_2O$, WO_3, and Pt/C, respectively, in the first cycle. The Tafel slope and exchange current density were, respectively, smaller and larger with WO_3 nanoplates than those of several other chalcogenides reported recently (Table S1, Supporting Information) for the HER. After 4000 CV cycles, the Tafel slope was found to be further decreased while the exchange current density increased for $WO_3 \cdot H_2O$ (Table 1). The estimated Tafel slopes suggested the Volmer−Tafel HER mechanism of these electrocatalysts.[32] The superior HER activity of W-based hydroxide and oxide to that of other recently studied materials (Table S1, Supporting Information) makes it a potential candidate for hydrogen generation.

To understand the better HER performance of WO_3 than that of $WO_3 \cdot H_2O$, the electrochemical active surface area (ECSA) was calculated from the electrochemical double layer capacitance measurement using eq 1.[33,34]

$$\mathrm{ECSA} = \frac{C_{dl}}{C_s} \tag{1}$$

where C_{dl} is the electrochemical double layer capacitance and C_s refers the specific electrochemical double layer capacitance of an atomically smooth surface (typically 15−50 μF cm^{-2}).[34] In the present case, the value of C_s is 30 μF cm^{-2} for all the electrodes in 0.5 M H_2SO_4 electrolyte. C_{dl} was calculated by measuring the CVs at different scan rates in the nonfaradaic region. Figure 5a,b shows the CVs of $WO_3 \cdot H_2O$ and WO_3

DOI: 10.1021/acsomega.7b01151
ACS Omega 2017, 2, 7039−7047

nanoplates at different scan rates (10−100 mV s^{-1}) in 0.5 M H_2SO_4 electrolyte, respectively. The capacitive currents for $WO_3·H_2O$ and WO_3 nanoplates at 0.7 V versus the reversible hydrogen electrode (RHE) were plotted as a function of scan rates (Figure 5c) and their slope is known as C_{dl}. The ECSA (and C_{dl}) of $WO_3·H_2O$ and WO_3 nanoplates was measured to be 1.0 cm^2 (0.03 mF) and 2.83 cm^2 (0.085 mF), respectively. The larger ECSA of WO_3 nanoplates clearly indicates more active sites in them, which resulted in higher HER performance compared to that of $WO_3·H_2O$ nanoplates. Furthermore, the specific activity (SA) of $WO_3·H_2O$ and WO_3 nanoplates was calculated to compare their intrinsic catalytic performance by normalizing the HER current density to the specific surface area (Figure S4, Supporting Information) as per eq 2.[35,36]

$$\mathrm{SA} = \frac{j}{10 \times m \times S_{\mathrm{BET}}} \quad (2)$$

where SA stands for specific activity (mA cm^{-2}), j refers to the current density (mA cm^{-2}) at 0.35 V (vs RHE), m stands for the catalyst loading mass (28.57 mg cm^{-2}), and S_{BET} is the Brunauer-Emmett-Teller surface area (m^2 g^{-1}). The SA values normalized to the specific surface area were calculated to be 2.58 and 5.38 in magnitude for $WO_3·H_2O$ and WO_3 nanoplates, respectively. This further confirms the higher HER performance of WO_3 nanoplates. The electrochemical impedance spectroscopy (EIS) study was carried out to understand the charge transfer behavior at the electrode/electrolyte interface. Figure 5d shows the Nyquist plots of $WO_3·H_2O$ and WO_3 nanoplates before and after 4000 CV cycles at an applied potential of 0.06 V versus the RHE in 0.5 M H_2SO_4. All the EIS spectra show semicircles and straight lines in the high-frequency and low-frequency regions, respectively. The diameter of the semicircles infers to the charge-transfer resistance (R_{ct}) at the electrode−electrolyte interface. A smaller semicircle confirms superiority of the electrode because of a smaller R_{ct}. The R_{ct} values for $WO_3·H_2O$ and WO_3 nanoplates were measured to be 9.3 and 5.5 Ω, respectively, by fitting the experimental data with an equivalent circuit model shown as an inset in Figure 5d. As expected, the R_{ct} value was decreased to 4.6 and 4.8 Ω for $WO_3·H_2O$ and WO_3 nanoplates, respectively, after 4000 cycle CV test. A smaller R_{ct} further validates an increased current density with the electrocatalysts after the stability test.

The quantitative estimation of hydrogen evolution was finally performed with WO_3 nanoplates using a gas chromatograph. The hydrogen generation rate was found to increase and reach 20.4 mmol·cm^{-2} in 10 h (Figure 6) with WO_3 nanoplates at −0.76 V versus the RHE in 0.5 M H_2SO_4. The repeated 4000 CV cycles (Figure S3, Supporting Information) and hydrogen generation for 10 h suggests the good stability of $WO_3·H_2O$ and WO_3 for the HER.

The HER investigation was further extended to a neutral medium using normal distilled water (pH 5.67). Figure 7a−c shows the LSV, Tafel, and chronoamperometry plots of $WO_3·H_2O$ and WO_3 nanoplates in water. The HER was found to begin at ∼0.5 V versus the RHE [−0.076 V vs saturated calomel electrode (SCE)] during the cathodic scan and HER current sharply increased below 0 V versus the RHE (−0.576 V vs SCE) in the presence of the catalyst, as shown in Figure 7a. As expected, WO_3 exhibited a higher HER activity in the neutral medium as well. The obtained HER current of 1.0 mA cm^{-2} at the overpotential of 15 mV in the first cycle is significantly lower than recently reported electrocatalysts studied in the PBS

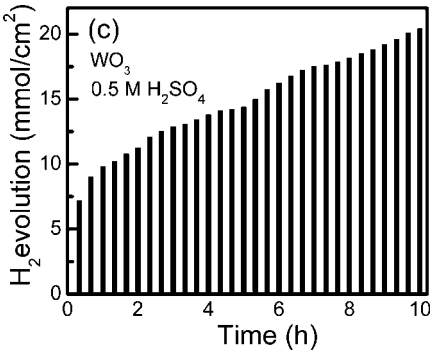

Figure 6. H_2 evolution measured by a gas chromatograph at −0.76 V vs the RHE using WO_3 nanoplates as the electrocatalyst and 0.5 M H_2SO_4 as the electrolyte.

electrolyte.[18,37] The Tafel slopes (and exchange current densities) of 49.75 mV dec^{-1} (1.0 mA cm^{-2}) and 43.43 mV dec^{-1} (1.15 mA cm^{-2}) were measured for $WO_3·H_2O$ and WO_3 nanoplates in the first cycle, respectively. The repeated CV cycles showed an increase in the HER current density of $WO_3·H_2O$ to the value obtained for WO_3 nanoplates in water as well (Figure S5a,b, Supporting Information). After 10 000 CV cycles, LSV collected with $WO_3·H_2O$ and WO_3 nanoplates revealed improved performance, that is, a higher current density (3.6 mA cm^{-2} at 15 mV overpotential for both $WO_3·H_2O$ and WO_3 nanoplates), smaller Tafel slope (30.0 mV dec^{-1} for $WO_3·H_2O$ and 41.98 mV dec^{-1} for WO_3), and higher exchange current density (1.5 mA cm^{-2} for $WO_3·H_2O$ and 1.1 mA cm^{-2} for WO_3) as shown in Figure S6 (Supporting Information) and Table 1. Similar to the HER study in acidic electrolyte, a higher positive current was found with $WO_3·H_2O$ than with WO_3 nanoplates prior to the onset of HER (Figure 7a), which is due to the oxidation of surface hydroxide. However, after repeated CV cycles, the positive current prior to the onset of the HER remained (Figure S6, Supporting Information), which suggests that further study is needed to understand this behavior. The chronoamperometry measurement further confirmed excellent stability of the electrocatalysts as studied for 20 h without a decrease in current (Figure 7c). The quantitative hydrogen generation was also measured using gas chromatography and was found to be 550 μmol·cm^{-2} in 10 h with WO_3 nanoplates at −0.42 V versus the RHE (or −1.0 V vs SCE) in distilled water (Figure 7d).

Surface Composition. Improvements in the HER performance of $WO_3·H_2O$ after repeated CV cycles is attributed to its surface modification to WO_3. The change in the surface composition was confirmed by X-ray photoelectron spectroscopic (XPS) and Auger electron spectroscopic (AES) measurements. Figure 8 shows the W 4f and O 1s region XPS spectra of $WO_3·H_2O$, $WO_3·H_2O$ after repeated CV cycles (in 0.5 M H_2SO_4), and WO_3. The W 4f binding energy positions are well-matched to the literature values.[38,39] The two O 1s XPS peaks at ∼530.5 and ∼531.7 eV are assigned to oxide and surface hydroxide, respectively.[39] The W and O atomic compositions estimated using CasaXPS software are presented in Table 2, which clearly indicate the change in the surface composition of $WO_3·H_2O$ to WO_3 after CV cycles. Figure S7 (Supporting Information) shows the AES spectra of $WO_3·H_2O$, $WO_3·H_2O$ after CV cycles (in 0.5 M H_2SO_4), and WO_3. The surface composition (Table 2) measured by AES correlates the XPS results and confirmed the surface oxidation of $WO_3·H_2O$

DOI: 10.1021/acsomega.7b01151
ACS Omega 2017, 2, 7039−7047

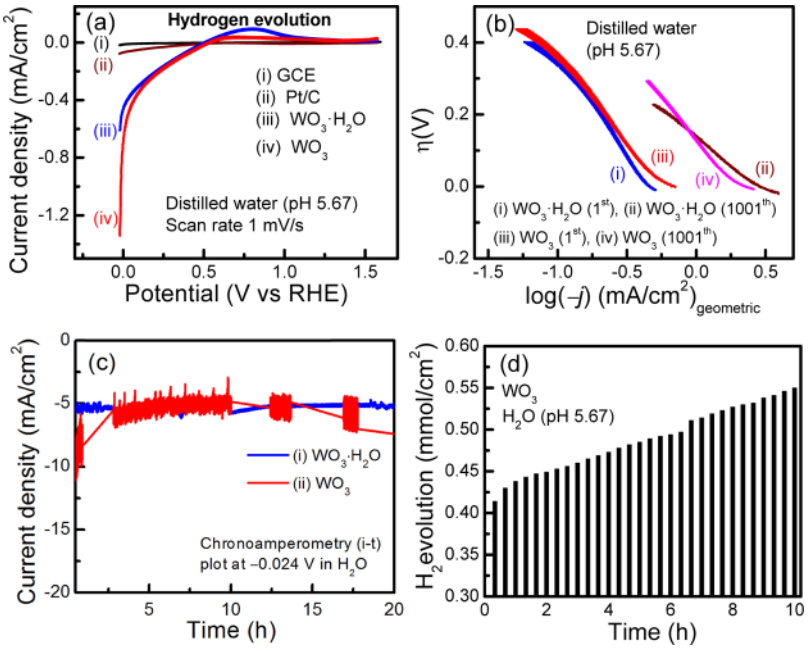

Figure 7. (a) LSV, (b) Tafel plots, and (c) chronoamperometry plots of $WO_3{\cdot}H_2O$ and WO_3 nanoplates for hydrogen evolution in distilled water at pH 5.67. (d) H_2 evolution measured by a gas chromatograph at −0.76 V vs the RHE using WO_3 nanoplates as the electrocatalyst and distilled water as the electrolyte.

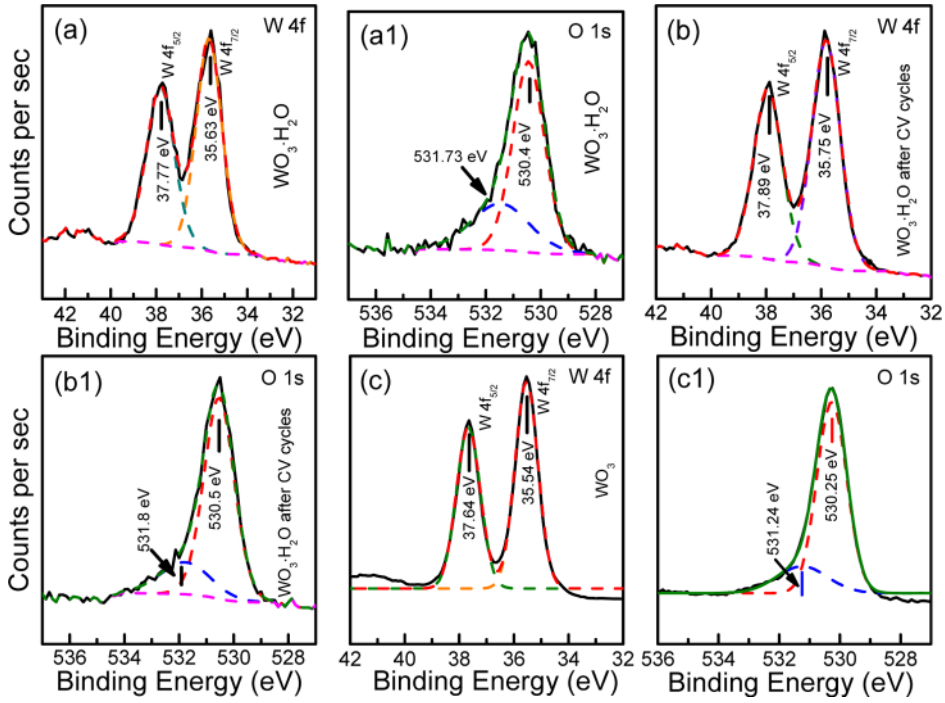

Figure 8. (a–c) W 4f and (a1–c1) O 1s region XPS spectra of (a) $WO_3{\cdot}H_2O$ nanoplates, (b) $WO_3{\cdot}H_2O$ nanoplates after 4000 CV cycles in 0.5 M H_2SO_4, and (c) WO_3 nanoplates.

to WO_3 during electrochemical CV cycles. This signifies the important role of room temperature synthesized $WO_3{\cdot}H_2O$ nanoplates for the HER. However, the XRD pattern (not shown) of $WO_3{\cdot}H_2O$ after CV cycles showed no change in its phase, thus indicating the surface modification only.

DFT Study. The mechanism of hydrogen evolution was further investigated using periodic plane wave DFT calculations on the (200) plane of the $P2_1/n$ monocline phase of WO_3 nanoplates as per experimental observation and their thermodynamic stability[40] and compared with those of the well-established Pt(111) catalyst.[41] The protons adsorbed on the hcp site of Pt(111) with the Pt–H bond distance of 1.912, 1.886, and 1.872 Å whereas 0.98 Å atop WO_3(200). The reaction coordinates for proton adsorption followed by its recombination ($H + e^- \rightarrow H^* \rightarrow 1/2H_2$) have been reported to be the indicator of HER catalyst activity.[42] Therefore, energy landscapes indicating the above reactions were developed as shown in Figure 9. The adsorption energy of proton on

DOI: 10.1021/acsomega.7b01151
ACS Omega 2017, 2, 7039–7047

Table 2. Surface Composition (Atomic Percentage) of $WO_3 \cdot H_2O$ Nanoplates before and after CV Cycles in 0.5 M H_2SO_4, and WO_3 Nanoplates Measured by XPS and AES

sample	atomic % by XPS		atomic % by AES	
	W %	O %	W %	O %
$WO_3 \cdot H_2O$	19.83	80.17	20.9	79.1
$WO_3 \cdot H_2O$ after CV cycles	24.47	75.53	22.4	77.6
WO_3	23.88	76.72	25.4	74.6

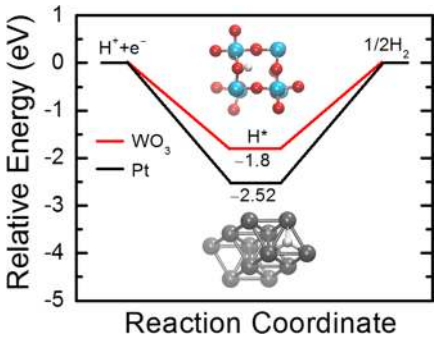

Figure 9. Calculated energy landscapes of the HER on WO_3(200) and Pt(111).

Pt(111) was calculated to be −2.52 eV matching the values calculated by Nobuhara et al.[43] Moreover, the proton adsorption energy on WO_3(200) was found to be −1.8 eV, which was lower than that of Pt, establishing the reason behind the superior HER performance of WO_3 as experimentally observed.

CONCLUSIONS

The present work spotlights the importance of hydroxide and oxide for the water-splitting reaction and generation of hydrogen. The inherent stability of oxides makes them highly suitable and efficient materials for the water-splitting reaction. The superior HER performance of $WO_3 \cdot H_2O$ and WO_3 was affirmed through high hydrogen evolution current densities and smaller Tafel slopes as demonstrated here. These catalysts also exhibited excellent durability in acidic and neutral electrolytes. The synthesis of $WO_3 \cdot H_2O$ at room temperature and its surface evolution to WO_3 during repeated electrochemical CV cycles were evidenced from surface characterization and electrochemical performances. In addition, the high hydrogen generation rate in acidic (20.4 mmol·cm^{-2}) and neutral (550 μmol·cm^{-2}) electrolytes as measured quantitatively demonstrated potential of these electrocatalysts for hydrogen generation through water splitting.

EXPERIMENTAL DETAILS

Chemicals. Tungsten (VI) chloride (WCl_6), platinum on carbon (Pt/C) (Sigma-Aldrich, USA), and ethanol (C_2H_5OH) and H_2SO_4 (Merck, India) were used for synthesis and activity tests. All chemicals were of analytical grade and used without further purification.

Synthesis of $WO_3 \cdot H_2O$ and WO_3 Nanoplates. In a typical synthesis, 40 mL (25 mM) of WCl_6 was prepared in ethanol and kept under ambient temperature (at ∼30 °C) for 1 h to obtain pine green color precipitate of $WO_3 \cdot H_2O$ nanoplates, which was washed with ethanol and dried at 60 °C for 4 h. WO_3 nanoplates were obtained by annealing $WO_3 \cdot H_2O$ nanoplates at 400 °C in a muffle furnace for 2 h under air and cooling the furnace naturally to room temperature.

Characterization. The crystal structures of the samples were examined with a PANalytical high-resolution XRD (PW 3040/60) operated at 40 kV and 30 mA with Cu Kα X-rays (1.54 Å). TG analysis was performed with a TA Instrument (TGA Q_{50}) under synthetic air (N_2/O_2 = 80:20) at a heating rate of 10 °C per min. The surface morphology of the as-synthesized $WO_3 \cdot H_2O$ and WO_3 powder was examined using a Carl Zeiss SUPRA 40 FESEM. The detailed microstructures of the samples were analyzed using a Tecnai G^2 TEM (FEI) at an accelerating voltage of 200 kV. The surface analysis of the samples was carried out by XPS using a PHI 5000 VersaProbe II scanning XPS microprobe with a monochromatic Al Kα source (1486.6 eV). The AES measurements were performed with a scanning Auger nanoprobe (PHI 710, ULAC-PHI Inc.) equipped with a coaxial cylindrical mirror analyzer.

Electrochemical Study. The HER activity of the as-synthesized catalysts was studied using a BioLogic SP-150 potentiostat with Pt-foil as the counter electrode, SCE as the reference electrode, and a GCE coated with the catalyst as the working electrode. Prior to loading the catalyst, the GCE was cleaned by polishing with alumina powder and sonicating in distilled water and ethanol. A slurry was prepared by sonicating the catalyst powder ($WO_3 \cdot H_2O$ or WO_3 nanoplates) in a mixture of distilled water (10 mg mL^{-1}) and one drop of diluted polytetrafluoroethylene (PTFE) (10 μL of 1% PTFE dispersion) for 30 min. Then, 50 μL of slurry was coated on the GCE by drop-cast and dried under vacuum overnight. The electrochemical measurements such as LSV and CV were carried out with a three-electrode system in 0.5 M H_2SO_4 electrolyte at a scan rate of 1−100 mV s^{-1}. The HER study was also performed in a neutral electrolyte using distilled water (pH 5.67). The electrode potential was calibrated with respect to the RHE by using the equation, E(RHE) = E(SCE) + 0.241 + 0.0591 pH. Stabilities of the as-synthesized electrocatalysts were measured by chronoamperometry for 20 h at a selected applied potential. The hydrogen generation rate was measured using a gas chromatograph (7890B, Agilent Technologies) both in acidic (0.5 M H_2SO_4) and neutral electrolytes (distilled water, pH 5.67) at −0.36 V and −0.42 V versus the RHE, respectively.

DFT Calculations. The HER mechanism was analyzed using DFT calculations on the (200) plane of $P2_1/n$ monoclinic WO_3 following the experimental observation. DFT calculations were implemented with a Quantum ESPRESSO package.[44] For optimization, a 2 × 2 surface unit cell was used with three layers while freezing bottom two layers. To avoid the interaction of the adsorbate and periodic image of the slab, a vacuum of 10 Å was incorporated. Plane wave self-consistent field calculations were carried out with the Perdew−Burke−Ernzerhof exchange−correlation functional,[42] and ultrasoft pseudopotentials were used. For the wave functions (and charge densities), a kinetic energy cutoff of 37 Ry (370 Ry) was used. The convergence threshold of 1 × 10^{-6} arb units and 2 × 2 × 1 k-mesh were used for energy and Brillouin zone sampling, respectively. DFT analysis was also done with a stable (111) plane of Pt within a Pt 2 × 2 super cell. A comparative energy landscape for the reaction $H^+ + e^- \rightarrow H^*$ was developed for the synthesized catalyst and the established Pt catalyst to corroborate the difference in their activities.

DOI: 10.1021/acsomega.7b01151
ACS Omega 2017, 2, 7039−7047

■ ASSOCIATED CONTENT

Supporting Information

The Supporting Information is available free of charge on the ACS Publications website at DOI: 10.1021/acsomega.7b01151.

TEM images, EDX mapping, CVs, N_2 adsorption−desorption isotherms, and AES spectra (PDF)

■ AUTHOR INFORMATION

Corresponding Author

*E-mail: deb@matsc.iitkgp.ernet.in (D.P.).

ORCID

Parag A. Deshpande: 0000-0002-2445-5873

Debabrata Pradhan: 0000-0003-3968-9610

Notes

The authors declare no competing financial interest.

■ ACKNOWLEDGMENTS

This work was supported by the Science and Engineering Research Board of India through grant number SB/S1/IC-15/2013.

■ REFERENCES

(1) Chow, J.; Kopp, R. J.; Portney, P. R. Energy Resources and Global Development. *Science* **2003**, *302*, 1528−1531.

(2) Turner, J. A. Sustainable Hydrogen Production. *Science* **2004**, *305*, 972−974.

(3) Jin, H.; Wang, J.; Su, D.; Wei, Z.; Pang, Z.; Wang, Y. In situ Cobalt−Cobalt Oxide/N-Doped Carbon Hybrids As Superior Bifunctional Electrocatalysts for Hydrogen and Oxygen Evolution. *J. Am. Chem. Soc.* **2015**, *137*, 2688−2694.

(4) Greeley, J.; Jaramillo, T. F.; Bonde, J.; Chorkendorff, I.; Nørskov, J. K. Computational High-throughput Screening of Electrocatalytic Materials for Hydrogen Evolution. *Nat. Mater.* **2006**, *5*, 909−913.

(5) Wu, M.; Shen, P. K.; Wei, Z.; Song, S.; Nie, M. High Activity PtPd-WC/C Electrocatalyst for Hydrogen Evolution Reaction. *J. Power Sources* **2007**, *166*, 310−316.

(6) Chen, W.-F.; Sasaki, K.; Ma, C.; Frenkel, A. I.; Marinkovic, N.; Muckerman, J. T.; Zhu, Y.; Adzic, R. R. Hydrogen-Evolution Catalysts Based on Non-Noble Metal Nickel-Molybdenum Nitride Nanosheets. *Angew. Chem., Int. Ed.* **2012**, *51*, 6131−6135.

(7) Gordon, R. B.; Bertram, M.; Graedel, T. E. Metal Stocks and Sustainability. *Proc. Natl. Acad. Sci. U.S.A.* **2006**, *103*, 1209−1214.

(8) Li, Y.; Wang, H.; Xie, L.; Liang, Y.; Hong, G.; Dai, H. MoS_2 Nanoparticles Grown on Graphene: An Advanced Catalyst for the Hydrogen Evolution Reaction. *J. Am. Chem. Soc.* **2011**, *133*, 7296−7299.

(9) Chen, Z.; Cummins, D.; Reinecke, B. N.; Clark, E.; Sunkara, M. K.; Jaramillo, T. F. Core−shell MoO_3−MoS_2 Nanowires for Hydrogen Evolution: A Functional Design for Electrocatalytic Materials. *Nano Lett.* **2011**, *11*, 4168−4175.

(10) Kibsgaard, J.; Chen, Z.; Reinecke, B. N.; Jaramillo, T. F. Engineering the Surface Structure of MoS_2 to Preferentially Expose Active Edge Sites for Electrocatalysis. *Nat. Mater.* **2012**, *11*, 963−969.

(11) Lukowski, M. A.; Daniel, A. S.; Meng, F.; Forticaux, A.; Li, L.; Jin, S. Enhanced Hydrogen Evolution Catalysis from Chemically Exfoliated Metallic MoS_2 Nanosheets. *J. Am. Chem. Soc.* **2013**, *135*, 10274−10277.

(12) Voiry, D.; Salehi, M.; Silva, R.; Fujita, T.; Chen, M.; Asefa, T.; Shenoy, V. B.; Eda, G.; Chhowalla, M. Conducting MoS_2 Nanosheets as Catalysts for Hydrogen Evolution Reaction. *Nano Lett.* **2013**, *13*, 6222−6227.

(13) Voiry, D.; Yamaguchi, H.; Li, J.; Silva, R.; Alves, D. C. B.; Fujita, T.; Chen, M.; Asefa, T.; Shenoy, V. B.; Eda, G.; Chhowalla, M. Enhanced Catalytic Activity in Strained Chemically Exfoliated WS_2 Nanosheets for Hydrogen Evolution. *Nat. Mater.* **2013**, *12*, 850−855.

(14) Yang, J.; Voiry, D.; Ahn, S. J.; Kang, D.; Kim, A. Y.; Chhowalla, M.; Shin, H. S. Two-Dimensional Hybrid Nanosheets of Tungsten Disulfide and Reduced Graphene Oxide as Catalysts for Enhanced Hydrogen Evolution. *Angew. Chem., Int. Ed.* **2013**, *52*, 13751−13754.

(15) Cheng, L.; Huang, W.; Gong, Q.; Liu, C.; Liu, Z.; Li, Y.; Dai, H. Ultrathin WS_2 Nanoflakes as a High-Performance Electrocatalyst for the Hydrogen Evolution Reaction. *Angew. Chem., Int. Ed.* **2014**, *53*, 7860−7863.

(16) Choi, C. L.; Feng, J.; Li, Y.; Wu, J.; Zak, A.; Tenne, R.; Dai, H. WS_2 Nanoflakes from Nanotubes for Electrocatalysis. *Nano Res.* **2013**, *6*, 921−928.

(17) Wang, H.; Kong, D.; Johanes, P.; Cha, J. J.; Zheng, G.; Yan, K.; Liu, N.; Cui, Y. $MoSe_2$ and WSe_2 Nanofilms with Vertically Aligned Molecular Layers on Curved and Rough Surfaces. *Nano Lett.* **2013**, *13*, 3426−3433.

(18) Andreiadis, E. S.; Jacques, P.-A.; Tran, P. D.; Leyris, A.; Chavarot-Kerlidou, M.; Jousselme, B.; Matheron, M.; Pécaut, J.; Palacin, S.; Fontecave, M.; Artero, V. Molecular Engineering of a Cobalt-based Electrocatalytic Nanomaterial for H_2 Evolution under Fully Aqueous Conditions. *Nat. Chem.* **2013**, *5*, 48−53.

(19) Karunadasa, H. I.; Chang, C. J.; Long, J. R. A Molecular Molybdenum-oxo Catalyst for Generating Hydrogen from Water. *Nature* **2010**, *464*, 1329−1333.

(20) Helm, M. L.; Stewart, M. P.; Bullock, R. M.; DuBois, M. R.; DuBois, D. L. A Synthetic Nickel Electrocatalyst with a Turnover Frequency above 100,000 s-1 for H_2 Production. *Science* **2011**, *333*, 863−866.

(21) Guo, S.-Q.; Zhen, M.-M.; Sun, M.-Q.; Zhang, X.; Zhao, Y.-P.; Liu, L. Controlled Fabrication of Hierarchical WO_3·H_2O Hollow Microspheres for Enhanced Visible Light Photocatalysis. *RSC Adv.* **2015**, *5*, 16376−16385.

(22) Liu, B.; Wang, J.; Wu, J.; Li, H.; Li, Z.; Zhou, M.; Zuo, T. Controlled Fabrication of Hierarchical WO_3 Hydrates with Excellent Adsorption Performance. *J. Mater. Chem. A* **2014**, *2*, 1947−1954.

(23) Huang, J.; Xu, X.; Gu, C.; Yang, M.; Yang, M.; Liu, J. Large-scale Synthesis of Hydrated Tungsten Oxide 3D Architectures by a Simple Chemical Solution Route and Their Gas-sensing Properties. *J. Mater. Chem.* **2011**, *21*, 13283−13289.

(24) Kalantar-zadeh, K.; Vijayaraghavan, A.; Ham, M.-H.; Zheng, H.; Breedon, M.; Strano, M. S. Synthesis of Atomically Thin WO_3 Sheets from Hydrated Tungsten Trioxide. *Chem. Mater.* **2010**, *22*, 5660−5666.

(25) Liu, Y.; Li, Q.; Gao, S.; Shang, J. K. Template-free Solvothermal Synthesis of WO_3/WO_3 H_2O Hollow Spheres and Their Enhanced Photocatalytic Activity From the Mixture Phase Effect. *CrystEngComm* **2014**, *16*, 7493−7501.

(26) Daniel, M. F.; Desbat, B.; Lassegues, J. C.; Gerand, B.; Figlarz, M. Infrared and Raman Study of WO_3 Tungsten Trioxides and WO_3, xH_2O Tungsten Trioxide tydrates. *J. Solid State Chem.* **1987**, *67*, 235−247.

(27) Nayak, A. K.; Lee, S.; Choi, Y. I.; Yoon, H. J.; Sohn, Y.; Pradhan, D. Crystal Phase and Size-Controlled Synthesis of Tungsten Trioxide Hydrate Nanoplates at Room Temperature: Enhanced Cr(VI) Photoreduction and Methylene Blue Adsorption Properties. *ACS Sustainable Chem. Eng.* **2017**, *5*, 2741−2750.

(28) Popczun, E. J.; McKone, J. R.; Read, C. G.; Biacchi, A. J.; Wiltrout, A. M.; Lewis, N. S.; Schaak, R. E. Nanostructured Nickel Phosphide as an Electrocatalyst for the Hydrogen Evolution Reaction. *J. Am. Chem. Soc.* **2013**, *135*, 9267−9270.

(29) Wang, T.; Liu, L.; Zhu, Z.; Papakonstantinou, P.; Hu, J.; Li, M. Enhanced Electrocatalytic Activity for Hydrogen Evolution Reaction from Self-Assembled Monodispersed Molybdenum Sulfide Nanoparticles on an Au Electrode. *Energy Environ. Sci.* **2013**, *6*, 625−633.

(30) Xie, J.; Zhang, H.; Li, S.; Wang, R.; Sun, X.; Zhou, M.; Zhou, J.; Lou, X. W.; Xie, Y. Defect-Rich MoS_2 Ultrathin Nanosheets with Additional Active Edge Sites for Enhanced Electrocatalytic Hydrogen Evolution. *Adv. Mater.* **2013**, *25*, 5807−5813.

(31) Phuruangrat, A.; Ham, D. J.; Hong, S. J.; Thongtem, S.; Lee, J. S. Synthesis of Hexagonal WO_3 Nanowires by Microwave-Assisted

DOI: 10.1021/acsomega.7b01151
ACS Omega 2017, 2, 7039−7047

Hydrothermal Method and Their Electrocatalytic Activities for Hydrogen Evolution Reaction. *J. Mater. Chem.* **2010**, *20*, 1683−1690.
(32) Conway, B. E.; Tilak, B. V. Interfacial Processes Involving Electrocatalytic Evolution and Oxidation of H_2, and the Role of Chemisorbed H. *Electrochim. Acta* **2002**, *47*, 3571−3594.
(33) Benck, J. D.; Chen, Z.; Kuritzky, L. Y.; Forman, A. J.; Jaramillo, T. F. Amorphous Molybdenum Sulfide Catalysts for Electrochemical Hydrogen Production: Insights into The Origin of Their Catalytic Activity. *ACS Catal.* **2012**, *2*, 1916−1923.
(34) Bikkarolla, S. K.; Papakonstantinou, P. $CuCo_2O_4$ Nanoparticles on Nitrogenated Graphene as Highly Efficient Oxygen Evolution Catalyst. *J. Power Sources* **2015**, *281*, 243−251.
(35) Huang, J.; Chen, J.; Yao, T.; He, J.; Jiang, S.; Sun, Z.; Liu, Q.; Cheng, W.; Hu, F.; Jiang, Y.; Pan, Z.; Wei, S. CoOOH Nanosheets with High Mass Activity for Water Oxidation. *Angew. Chem., Int. Ed.* **2015**, *54*, 8722−8727.
(36) Song, F.; Hu, X. Exfoliation of Layered Double Hydroxides for Enhanced Oxygen Evolution Catalysis. *Nat. Commun.* **2014**, *5*, 4477.
(37) Cobo, S.; Heidkamp, J.; Jacques, P.-A.; Fize, J.; Fourmond, V.; Guetaz, L.; Jousselme, B.; Ivanova, V.; Dau, H.; Palacin, S.; Fontecave, M.; Artero, V. A Janus Cobalt-based Catalytic Material for Electro-splitting of Water. *Nat. Mater.* **2012**, *11*, 802−807.
(38) Nayak, A. K.; Ghosh, R.; Santra, S.; Guha, P. K.; Pradhan, D. Hierarchical Nanostructured WO_3−SnO_2 for Selective Sensing of Volatile Organic Compounds. *Nanoscale* **2015**, *7*, 12460−12473.
(39) Baek, Y.; Yong, K. Controlled Growth and Characterization of Tungsten Oxide Nanowires Using Thermal Evaporation of WO_3 Powder. *J. Phys. Chem. C* **2007**, *111*, 1213−1218.
(40) Li, Y. H.; Liu, P. F.; Pan, L. F.; Wang, H. F.; Yang, Z. Z.; Zheng, L. R.; Hu, P.; Zhao, H. J.; Gu, L.; Yang, H. G. Local Atomic Structure Modulations Activate Metal Oxide as Electrocatalyst for Hydrogen Evolution in Acidic Water. *Nat. Commun.* **2015**, *6*, 8064.
(41) Skúlason, E.; Karlberg, G. S.; Rossmeisl, J.; Bligaard, T.; Greeley, J.; Jónsson, H.; Nørskov, J. K. Density Functional Theory Calculations for the Hydrogen Evolution Reaction in an Electrochemical Double Layer on the Pt(111) Electrode. *Phys. Chem. Chem. Phys.* **2007**, *9*, 3241−3250.
(42) Perdew, J. P.; Burke, K.; Ernzerhof, M. Generalized Gradient Approximation Made Simple. *Phys. Rev. Lett.* **1996**, *77*, 3865−3868.
(43) Nobuhara, K.; Nakanishi, H.; Kasai, H.; Okiji, A. Interactions of Atomic Hydrogen with Cu(111), Pt(111), and Pd(111). *J. Appl. Phys.* **2000**, *88*, 6897−6901.
(44) Giannozzi, P.; et al. QUANTUM ESPRESSO: A Modular and Open-source Software Project for Quantum Simulations of Materials. *J. Phys.: Condens. Matter* **2009**, *21*, 395502.

DOI: 10.1021/acsomega.7b01151
ACS Omega 2017, 2, 7039−7047